Suppressed Magnetic Circular Dichroism and Valley-Selective Magnetoabsorption due to the Effective Mass Anisotropy in Bismuth

Pieter J. de Visser,[1,2,*] Julien Levallois,[1,†] Michaël K. Tran,[1] Jean-Marie Poumirol,[1] Ievgeniia O. Nedoliuk,[1] Jérémie Teyssier,[1] Ctirad Uher,[3] Dirk van der Marel,[1] and Alexey B. Kuzmenko[1,‡]

[1]*Department of Quantum Matter Physics, University of Geneva, Geneva 1211, Switzerland*

[2]*Kavli Institute of NanoScience, Faculty of Applied Sciences, Delft University of Technology, Lorentzweg 1, 2628 CJ Delft, Netherlands*

[3]*Department of Physics, University of Michigan, Ann Arbor, Michigan 48109, USA*

(Received 20 January 2016; revised manuscript received 12 April 2016; published 29 June 2016)

We measure the far-infrared reflectivity and Kerr angle spectra on a high-quality crystal of pure semimetallic bismuth as a function of magnetic field, from which we extract the conductivity for left- and right-handed circular polarizations. The high spectral resolution allows us to separate the intraband Landau level transitions for electrons and holes. The hole transition exhibits 100% magnetic circular dichroism; it appears only for one polarization as expected for a circular cyclotron orbit. However, the dichroism for electron transitions is reduced to only $13 \pm 1\%$, which is quantitatively explained by the large effective mass anisotropy of the electron pockets of the Fermi surface. This observation is a signature of the mismatch between the metric experienced by the photons and the electrons. It allows for a contactless measurement of the effective mass anisotropy and provides a direction towards valley polarized magnetooptical pumping with elliptically polarized light.

DOI: 10.1103/PhysRevLett.117.017402

Circular dichroism, the property of materials to interact differently with left and right circularly polarized light, is associated with symmetry breaking due to, e.g., molecular chirality, spontaneous magnetization, or an external magnetic field. A charged particle in a magnetic field moves in a circular orbit perpendicular to that field. Radiation propagating parallel to the field is only absorbed by that particle for right or left circular polarization, leading to 100% magnetic circular dichroism. In condensed matter, the behavior of charge carriers in a lattice is described using an effective mass, which can be very different from the free-electron mass, but also strongly anisotropic [1]. In the latter case the cyclotron orbits become elliptical, which, as we will show, strongly reduces the magnetic circular dichroism. The reduction of magnetic circular dichroism can thus be regarded as a manifestation of the mismatch between the metric experienced by the photons (isotropic) and the electrons (anisotropic), which becomes apparent when they interact [2–4]. As a consequence, elliptically polarized light with the same ellipticity as an electron pocket can cause a 100% valley polarized magnetooptical absorption.

Bismuth is a canonical semimetal that possesses a rich electronic structure with a strong spin-orbit interaction, low carrier density, long mean-free path, and small cyclotron mass [5–8]. Important phenomena such as the Seebeck effect [9], Nernst effect [10], and quantum oscillations [11,12] were discovered in bismuth. More recently a valley-ferromagnetic state [13], a valley-nematic Fermi liquid state [14], a valley dependent density of states [15], an avoided Lifshitz type semimetal-semiconductor transition [16], and topological edge states [17] have been revealed. The Fermi surface of bismuth is highly anisotropic [Fig. 1(a)]. A hole pocket is oriented along the trigonal axis, where the bands are almost parabolic. Three electron pockets are tilted 6° from the plane perpendicular to the trigonal axis and have a Dirac-like band dispersion. In this plane the dielectric function is isotropic. A magnetic field parallel to the trigonal axis combined with light propagating along the same axis therefore presents an ideal case to measure the dichroism in relation to the effective mass. For holes the mass is isotropic in the plane whereas for electrons it is strongly anisotropic (a factor > 200 [18]), leading to a strong dichroism contrast between electron and hole transitions, as schematically shown in Fig. 1(b). Quite a few (far-)infrared magnetooptical studies have been carried out to study band parameters, Landau level transitions, and selection rules in Bi [19–30]. However, these were limited to selected wavelengths or, when spectroscopy was done, the polarization dependence was not measured [31,32].

Here, we present measurements of the far-infrared reflectivity and Kerr angle spectra on a high-quality crystal of pure bismuth as a function of magnetic field (0–7 T, applied along the trigonal axis), from which the conductivity for left-handed (σ_-) and right-handed (σ_+) circular polarizations (seen from the source) are derived. The high spectral resolution (1 cm^{-1}) enables distinguishing the intraband Landau level transitions for electrons and holes using their different magnetic field dependence. The observed hole transition shows maximum magnetic circular dichroism; it appears only for one polarization, because the effective mass for holes is isotropic in this plane. However, the magnetic circular dichroism $A = (\sigma_+ - \sigma_-)/(\sigma_+ + \sigma_-)$ for electron transitions is strongly reduced. The observed dichroism for

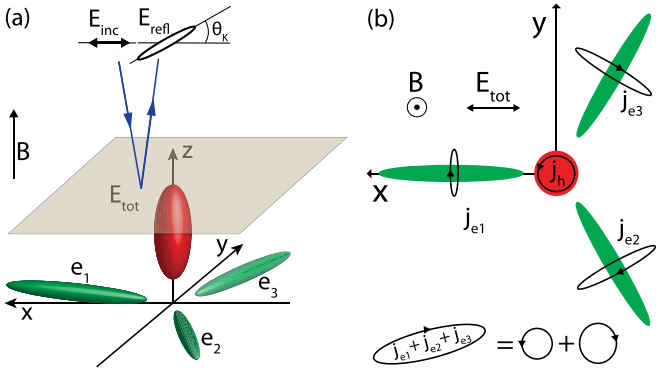

FIG. 1. (a) Schematic representation of the interaction of charge carriers in bismuth with light. The Fermi surface of bismuth is sketched in the interior of the sample, with a hole pocket (red) oriented along the trigonal (z) axis (inspired by Ref. [18]). Three electron pockets (green) are oriented almost perpendicularly to the trigonal axis (with a 6° tilt), rotated by 120° with respect to each other. A magnetic field is applied along the z axis. Radiation with linear polarization (E_{inc}) is propagating almost parallel to the field. Close to the intraband resonances the light reflects (E_{refl}) with an elliptical polarization and is rotated by the Kerr angle θ_K. (b) Top view on the trigonal plane. The effective electric field E_{tot} in the crystal generates currents (both in real space) in the different pockets (in reciprocal space) according to $j = \sigma E_{\mathrm{tot}}$. The current in the hole pocket results in complete magnetic circular dichroism. The sum of the currents in the electron pockets shows strongly reduced circular dichroism due to the large effective mass anisotropy (bottom).

the electron transitions of 0.13 ± 0.01 agrees with calculations, which include the strong effective mass anisotropy of the three electron pockets.

The magnetooptical reflectivity and Kerr angle spectra were measured in a split-coil superconducting magnet attached to a Fourier transform spectrometer. The Bi crystal, with 99.9999% purity, was cleaved in liquid nitrogen along the natural cleavage plane perpendicular to the trigonal axis. We performed spectroscopy on a freshly cleaved, untreated surface, which shows only atomic height variations over large parts of the surface (see the Supplemental Material [33]). The measurements were performed at 5 K with radiation at nearly normal angle of incidence (8°). The magnetic field was applied along the trigonal axis and thus almost parallel to the propagation of the light (Faraday geometry).

The reflectivity $R(\omega, B)$ and Kerr angle $\theta_K(\omega, B)$ were measured in a single measurement run using two polarizers, one before and one after the sample. The absolute reflectivity was measured with a double reference method. At every magnetic field the spectrum on the sample and on a gold reference mirror was taken. The measurements were repeated after *in situ* evaporation of a gold layer on the sample. The Kerr angle was measured using the fast protocol explained in Ref. [34]. More details on the experiment are given in the Supplemental Material [33], together with plots of the measured $R(\omega)$ and $\theta_K(\omega)$.

We employ a generalized magnetooptical Kramers-Kronig analysis (MOKKA) to calculate σ_- and σ_+ from the measurements [34]. $R(\omega)$ and $\theta_K(\omega)$ are initially fitted using a sum of Lorentzians, which relies on complementary ellipsometry data for the high frequencies (not shown). Subsequently, two independent Kramers-Kronig-consistent variational functions are added to the initial fit, and adjusted to simultaneously reproduce $R(\omega)$ and $\theta_K(\omega)$, resulting in model-independent $\sigma_+(\omega)$ and $\sigma_-(\omega)$, which are shown in Figs. 2(a) and 2(b) for the energy range where intraband Landau-level transitions occur. The transition energies, which are marked on the peak positions in Figs. 2(a) and 2(b), are plotted with the same symbols in Figs. 3(c) and 3(d) as a function of magnetic field. Before we can address the magnetic circular dichroism, we first need to identify the various transitions that occur.

The hole band of the Brillouin zone in Bi is usually considered to be parabolic and therefore the hole Landau levels are equidistant in energy. Because of the influence of outside bands and a strong spin-orbit coupling, a Zeeman-like term needs to be added, resulting in the Landau level energies for the hole band E_h as a function of magnetic field B at $k_z = 0$ given by [18]

$$E_h(n, s, B) = E_0 + \Delta - \left(n + \frac{1}{2}\right)\frac{\hbar e B}{M_c} + sG\mu_B B, \quad (1)$$

where $n = 0, 1, \ldots$ is the Landau level index, $s = \pm\frac{1}{2}$ is the spin quantum number, E_0 is the energy separation between the top of the hole valence band and the bottom of the

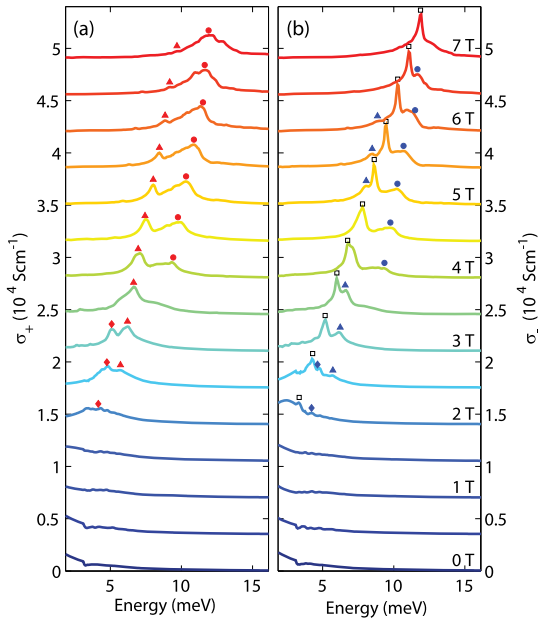

FIG. 2. (a), (b) The real part of the measured conductivity for right and left circularly polarized light, σ_+ and σ_-, as a function of the photon energy. The magnetic field steps are 0.5 T and the same color coding applies to both panels. The curves are displaced for clarity. The symbols at each peak correspond to Figs. 3(c) and 3(d).

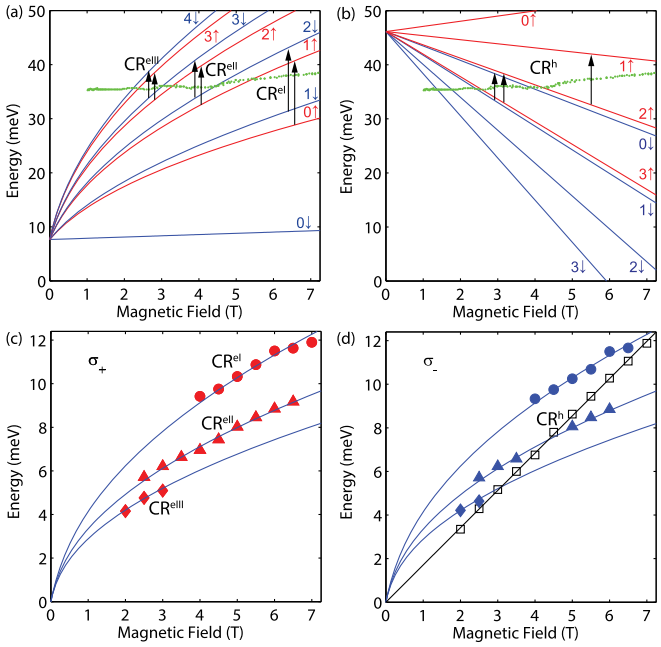

FIG. 3. Energies of the Landau levels for electrons (a) and holes (b), labeled with their n and spin. The Fermi level (green dots) is taken from Ref. [18]. The relevant transitions for this experiment are indicated as arrows. For electrons, transitions for spin up from level n have the same energy as transitions for spin down from level $n+1$. For holes all transitions have the same energy. (c), (d) Measured energies of the Landau level transitions as a function of magnetic field for σ_+ and σ_-. The different symbols mark experimental points of the different series of transitions. The lines represent the theoretical field dependence as given by Eq. (1) (holes) and Eq. (2) (electrons).

electron conduction band ($E_0 = 38.5$ meV [23]), e is the elementary charge, M_c is the cyclotron mass, $\hbar$ is Planck's reduced constant, μ_B is the Bohr magneton, and G is the g factor for holes. The resulting energy levels are shown in Fig. 3(b). The transition energy between levels with different n is thus linear in B.

For the electron pockets the gap separating the valence and conduction band is small ($2\Delta = 15.3$ meV [18]) giving rise to a strongly relativistic Dirac-like band structure. Although the detailed electronic structure of Bi is complicated, most of the magnetotransport data can be described using a two-band Dirac Hamiltonian, complemented with a Zeeman term, which approximately takes into account outside band effects [25]. This extended Dirac Hamiltonian leads to the following expression for the Landau levels in the conduction band [18,25]:

$$E_e(n,s,B) = \sqrt{\Delta^2 + 2\Delta\left(n + \frac{1}{2} + s\right)\frac{\hbar e B}{m_c}} + s g' \mu_B B, \tag{2}$$

with m_c the cyclotron mass and g' the electron g factor. The energy levels are shown in Fig. 3(a). Spin-conserving transitions between the electron Landau levels have a quasi-square-root dependence on B. In writing the transition energies [Eqs. (1) and (2)] we assumed that $k_z \approx 0$, since the Fermi pockets only span a small piece of k-space around the Fermi energy.

We can now identify the strong transition in σ_- with the linear field dependence [Fig. 3(d), open squares] as a hole transition with $\Delta n = -1$ and $\Delta s = 0$. We fit the theoretical field dependence to the data [black line in Fig. 3(d)], which results in $M_c = (0.0677 \pm 0.0002) m_0$, in excellent agreement with the literature [18]. Here, m_0 is the free electron mass.

The transitions marked in Figs. 3(c) and 3(d) as filled symbols correspond to three different electron transitions with $\Delta n = 1$, $\Delta s = 0$. Fits through the data points using Eq. (2), shown as blue lines in Figs. 3(c) and 3(d), give $m_c = (0.0135 \pm 0.0001) m_0$ based on $2\Delta = 15.3$ meV [18,35]. We note that the hole transition occurs more sharply in the spectra (Fig. 2) than the electron transitions because only the electron transitions are affected by a small spread in k_z [18]. The arrow in Fig. 4(a) marks an unidentified peak, which has a negligible spectral weight and is discussed in the Supplemental Material [33].

We have seen that the hole transition is only visible in σ_- as expected for a circular cyclotron orbit. It is striking that all the observed electron transitions in σ_+ also show up in σ_-. Figure 4(a) compares the measured $\sigma_+(\omega)$ and $\sigma_-(\omega)$ at 5.5 T. Apart from the strong dichroism at the hole peak, we observe that the spectral weight of the electron transitions is almost the same in $\sigma_+(\omega)$ and $\sigma_-(\omega)$. As we will now show, this is due to the strong effective mass anisotropy of the electron pockets.

To describe the anisotropy we first introduce a new coordinate system $\tilde{x}$ and $\tilde{y}$, in which the Fermi surface is isotropic, by using scaling coefficient α:

$$x \to \tilde{x} = \alpha^{-1/2} x, \qquad y \to \tilde{y} = \alpha^{1/2} y. \tag{3}$$

Formally, this is the same as transforming the effective mass and retaining the original metric:

$$m_x \to \tilde{m}_x = \alpha m_x, \qquad m_y \to \tilde{m}_y = \alpha^{-1} m_y. \tag{4}$$

The effective mass anisotropy is thus formally equivalent to a uniaxial stretching of the spatial metric [2,4,36]. The metric transformation conserves both the volume of the pocket and the cyclotron mass.

We proceed by considering the projection onto the trigonal plane of one electron pocket with its long axis parallel to the x axis [Fig. 1(b)]. The conductivity from this pocket $\hat{\sigma}_{e1}$ can be written as

$$\hat{\sigma}_{e1} = \begin{pmatrix} \tilde{\sigma}_{xx} & \tilde{\sigma}_{xy} \\ -\tilde{\sigma}_{xy} & \tilde{\sigma}_{yy} \end{pmatrix} = \begin{pmatrix} \alpha^{-1} s_{xx} & s_{xy} \\ -s_{xy} & \alpha s_{xx} \end{pmatrix}, \tag{5}$$

where s and $\tilde{\sigma}$ are the conductivities for, respectively, an isotropic and anisotropic pocket. The derivation of Eq. (5),

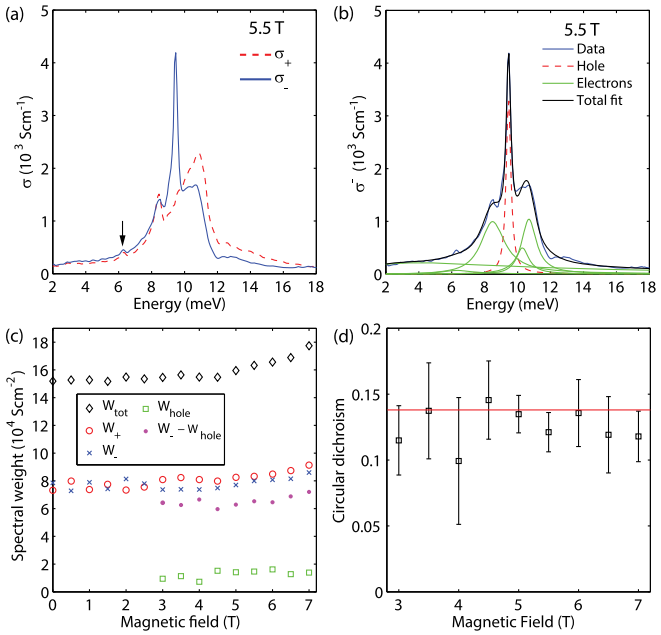

FIG. 4. (a) Comparison of σ_+ and σ_- as a function of energy measured at 5.5 T, showing the large dichroism for the hole transition together with the strongly reduced dichroism for the electron transitions. The tiny peak indicated with an arrow is discussed in the text. (b) Example of how the spectral weight for the hole transitions is derived for the σ_- spectrum at 5.5 T. We use a Lorentzian at each transition and a Drude term to account for the low frequency spectral weight. (c) The spectral weight of the intraband transitions, integrated over energies 0–25 meV as a function of magnetic field. The symbols denote the total spectral weight in $\sigma_+ + \sigma_-$ (diamonds), in σ_+ (circles), in σ_- (crosses), in the hole transition only (squares), and in σ_- when the hole spectral weight is subtracted (dots). (d) The magnetic circular dichroism ratio for the electron transitions at the magnetic fields where the hole peak can be subtracted. The line is the theoretical value based on the effective mass anisotropy of the electron pockets. The error bars are explained in the text.

for a general Hamiltonian, is given in the Supplemental Material [33]. The magnetic circular dichroism for the isotropic case is thus given by $A^s = (s_+ - s_-)/(s_+ + s_-)$ with $s_\pm = s_{xx} \pm i s_{xy}$. Using Eq. (5), the total electron conductivity is now obtained by adding the two remaining pockets, which are rotated using the rotation matrix $\hat{R}$ by $\pm 120°$: $\hat{\sigma} = \hat{\sigma}_{e1} + \hat{R}\hat{\sigma}_{e1}\hat{R}^{-1} + \hat{R}^{-1}\hat{\sigma}_{e1}\hat{R}$. In the circular basis, $\sigma_\pm = \sigma_{xx} \pm i\sigma_{xy}$, which leads to

$$\sigma_\pm = 3\left[\left(\frac{\alpha^{-1/2} \pm \alpha^{1/2}}{2}\right)^2 s_+ + \left(\frac{\alpha^{-1/2} \mp \alpha^{1/2}}{2}\right)^2 s_-\right]. \quad (6)$$

The total dichroism A can now be related to the effective mass anisotropy and is given by

$$A = \frac{\sigma_+ - \sigma_-}{\sigma_+ + \sigma_-} = \frac{2}{\alpha^{-1} + \alpha}\frac{s_+ - s_-}{s_+ + s_-} = \frac{2}{\alpha^{-1} + \alpha}A^s, \quad (7)$$

regardless of the form of A^s and valid for a general Hamiltonian and thus for parabolic and Dirac bands. For a circularly symmetric Fermi surface, $A = A^s$ and the dichroism is just that given by the transitions involved. In bismuth, we expect 100% dichroism for the hole transitions [Fig. 1(b)], which we experimentally observe in Figs. 2 and 4(a). For the electron transitions we also have $A^s = 1$, but the electron pockets are strongly elongated with $m_x = 0.257 m_0$ and $m_y = 0.00124 m_0$ ([18], which takes into account the 6° tilt) and thus $\alpha = \sqrt{m_x/m_y} = 14.4$. Therefore, we expect a strongly reduced dichroism, $A = 0.138$, for the electron transitions.

To derive the magnetic circular dichroism for electrons from the experimental data, we first need to subtract the spectral weight of the hole transition from σ_-. To that end we perform a fit using four Lorentzians and a small Drude term as shown in Fig. 4(b). Alternatively, the hole weight can be calculated from the knowledge of the shape of σ_+. The plotted hole weight is an average of both methods [33]. Figure 4(c) shows the spectral weight $W = \int_0^{25\ \mathrm{meV}} \sigma(\omega) d\omega$ (the intraband region) for σ_+, for σ_-, for $\sigma_+ + \sigma_-$, for the hole peak, and for σ_- with the hole peak subtracted. The increase of the total spectral weight above 4.5 T is related to the increase in carrier density at higher fields [18]. We can now derive the experimental dichroism for the electron pockets, which is shown in Fig. 4(d) and is the central result of this work. Error bars are estimated from the hole subtraction procedure [33]. The line is the theoretical expectation $A = 0.138$, which agrees well with the measurements. The weighted average over the magnetic fields is $A = 0.13 \pm 0.01$. We can thus distinguish Landau level transitions that happen at the same time in an isotropic hole valley and in an anisotropic electron valley from each other. Moreover, we can quantitatively relate the measured magnetic circular dichroism to the effective mass anisotropy.

Magnetic circular dichroism thus provides a contactless method to measure the effective mass anisotropy and could complement transport based techniques. To derive the dichroism, the anisotropy in the Hamiltonian has to be considered, in contrast to transport measurements where an isotropic mass model suffices (once the direction of the magnetic field is fixed) [4,18]. The high mass anisotropy presents light, which enters the crystal from vacuum with a large metric mismatch. The photons can therefore still probe the mass anisotropy, using the reduced circular dichroism. Intriguingly, electronic interactions can also strongly influence the effective metric of a material [3,4,37], which also plays a role in topological insulators, especially if they already have a band-mass anisotropy [38–42].

The above measurements and theory suggest that applying elliptically polarized light would lead to a highly valley-polarized magneto-absorption. If we consider light with an ellipticity matching the ellipticity of the cyclotron orbits but with opposite handedness, the absorbed power per unit volume in pocket $e1$ is given by [33]

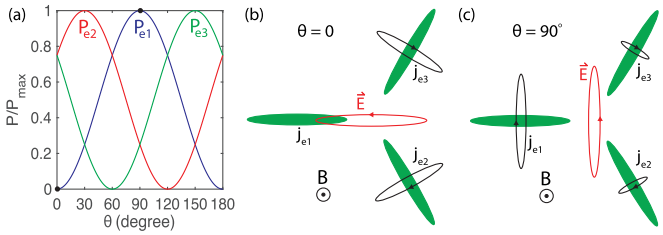

FIG. 5. (a) Relative power absorbed in each electron pocket for elliptically polarized light as a function of the azimuth angle of the polarization ellipse θ. (b),(c) Schematics of the valley-polarized magneto-absorption for $\theta = 0°$ and $\theta = 90°$, respectively.

$$P_{e1}(\theta) = P_{e1,\max}\sin^2\theta \tag{8}$$

with θ the angle between the long axis of the polarization ellipse and the x axis. Consequently, $P_{e2}(\theta) = P_{e1}(\theta + 60°)$ and $P_{e3}(\theta) = P_{e1}(\theta - 60°)$, which are plotted in Fig. 5(a). A 100% valley polarization (i.e., one valley does not absorb light) can thus be obtained at three angles $\theta = 0°, 60°, 120°$ (Fig. 5). This is a totally different approach to valleytronic applications in bismuth, as compared to previous suggestions where the magnetic field is rotated in the xy plane [14,43]. It provides another perspective to valleytronics in dichalcogenides, in which circularly polarized light is normally used [44–47], and to the proposed valley polarization in topological insulators using elliptical polarization [48].

We acknowledge B. Fauqué, K. Behnia, G. N. Kozhemyakin, and T. Giamarchi for discussions and M. Brandt, S. Zanos, D. Chablaix, D. Stricker, and I. Gaponenko for technical assistance. This research was supported by the Swiss National Science Foundation (Grant No. 200020-156615) and by the EU Graphene Flagship (Contract No. CNECT-ICT-604391 and 696656). P. J. de V. acknowledges support from a Niels Stensen Fellowship.

P. J. de V. and J. L. contributed equally to this work.

*p.j.devisser@tudelft.nl
†Julien.Levallois@unige.ch
‡Alexey.Kuzmenko@unige.ch

[1] C. Kittel, *Introduction to Solid State Physics*, 8th ed. (John Wiley & Sons, Inc., 2005).
[2] P. A. Wolff, J. Phys. Chem. Solids **25**, 1057 (1964).
[3] F. D. M. Haldane, Phys. Rev. Lett. **107**, 116801 (2011).
[4] B. Yang, Z. Papić, E. H. Rezayi, R. N. Bhatt, and F. D. M. Haldane, Phys. Rev. B **85**, 165318 (2012).
[5] M. H. Cohen and E. I. Blount, Philos. Mag. **5**, 115 (1960).
[6] L. A. Fal'kovsky, Usp. Fiz. Nauk **94**, 3 (1968).
[7] V. S. Édel'man, Usp. Fiz. Nauk **123**, 257 (1977).
[8] Y. Fuseya, M. Ogata, and H. Fukuyama, J. Phys. Soc. Jpn. **84**, 012001 (2015).
[9] T. J. Seebeck, Abh. Dtsch. Akad. Wiss. Berlin 265 (1823).
[10] A. v. Ettingshausen and W. Nernst, Ann. Phys. (Berlin) **265**, 343 (1886).
[11] L. Schubnikov and W. de Haas, Comm. Phys. Lab. Leiden **207d**, 35 (1930).
[12] W. J. de Haas and P. M. van Alphen, Comm. Phys. Lab. Leiden **212a**, 3 (1930).
[13] L. Li, J. G. Checkelsky, Y. S. Hor, C. Uher, A. F. Hebard, R. J. Cava, and N. P. Ong, Science **321**, 547 (2008).
[14] Z. Zhu, A. Collaudin, B. Fauqué, W. Kang, and K. Behnia, Nat. Phys. **8**, 89 (2012).
[15] R. Küchler, L. Steinke, R. Daou, M. Brando, K. Behnia, and F. Steglich, Nat. Mater. **13**, 461 (2014).
[16] N. P. Armitage, R. Tediosi, F. Lévy, E. Giannini, L. Forro, and D. van der Marel, Phys. Rev. Lett. **104**, 237401 (2010).
[17] I. K. Drozdov, A. Alexandradinata, S. Jeon, S. Nadj-Perge, H. Ji, R. J. Cava, B. A. Bernevig, and A. Yazdani, Nat. Phys. **10**, 664 (2014).
[18] Z. Zhu, B. Fauqué, Y. Fuseya, and K. Behnia, Phys. Rev. B **84**, 115137 (2011).
[19] B. Lax, J. G. Mavroides, H. J. Zeiger, and R. J. Keyes, Phys. Rev. Lett. **5**, 241 (1960).
[20] W. S. Boyle and A. D. Brailsford, Phys. Rev. **120**, 1943 (1960).
[21] R. N. Brown, J. G. Mavroides, and B. Lax, Phys. Rev. **129**, 2055 (1963).
[22] J. C. Burgiel and L. C. Hebel, Phys. Rev. **140**, A925 (1965).
[23] G. E. Smith, G. A. Baraff, and J. M. Rowell, Phys. Rev. **135**, A1118 (1964).
[24] G. A. Baraff, Phys. Rev. **137**, A842 (1965).
[25] M. Maltz and M. S. Dresselhaus, Phys. Rev. B **2**, 2877 (1970).
[26] R. L. Blewitt and A. J. Sievers, J. Low Temp. Phys. **13**, 617 (1973).
[27] M. P. Vecchi and M. S. Dresselhaus, Phys. Rev. B **9**, 3257 (1974).
[28] M. P. Vecchi, J. R. Pereira, and M. S. Dresselhaus, Phys. Rev. B **14**, 298 (1976).
[29] H. R. Verdún and H. D. Drew, Phys. Rev. B **14**, 1370 (1976).
[30] H. R. Verdún and H. D. Drew, Phys. Rev. B **15**, 5636 (1977).
[31] J. P. Omaggio, J. R. Meyer, C. A. Hoffman, A. DiVenere, X. J. Yi, C. L. Hou, H. C. Wang, J. B. Ketterson, G. K. Wong, and J. P. Heremans, Phys. Rev. B **48**, 11439 (1993).
[32] A. D. LaForge, A. Frenzel, B. C. Pursley, T. Lin, X. Liu, J. Shi, and D. N. Basov, Phys. Rev. B **81**, 125120 (2010).
[33] See Supplemental Material at http://link.aps.org/supplemental/10.1103/PhysRevLett.117.017402 for measurement details, additional measurement data, error analysis, and derivation of the circular dichroism and valley polarization.
[34] J. Levallois, I. O. Nedoliuk, I. Crassee, and A. B. Kuzmenko, Rev. Sci. Instrum. **86**, 033906 (2015).
[35] Based on only this data, Δ and m_c cannot be fitted independently.
[36] J. J. Quinn, Phys. Rev. **135**, A181 (1964).
[37] B. I. Halperin, P. A. Lee, and N. Read, Phys. Rev. B **47**, 7312 (1993).
[38] D. Hsieh, D. Qian, L. Wray, Y. Xia, Y. S. Hor, R. J. Cava, and M. Z. Hasan, Nature (London) **452**, 970 (2008).
[39] H. Zhang, C.-X. Liu, X.-L. Qi, X. Dai, Z. Fang, and S.-C. Zhang, Nat. Phys. **5**, 438 (2009).
[40] P. Dziawa, B. J. Kowalski, K. Dybko, R. Buczko, A. Szczerbakow, M. Szot, E. Lusakowska, T. Balasubramanian, B. M. Wojek, M. H. Berntsen, O. Tjernberg, and T. Story, Nat. Mater. **11**, 1023 (2012).

[41] M. Neupane, S.-Y. Xu, R. Sankar, N. Alidoust, G. Bian, C. Liu, I. Belopolski, T.-R. Chang, H.-T. Jeng, H. Lin, A. Bansil, F. Chou, and M. Z. Hasan, Nat. Commun. **5**, 3786 (2014).
[42] Y. Zhao, H. Liu, C. Zhang, H. Wang, J. Wang, Z. Lin, Y. Xing, H. Lu, J. Liu, Y. Wang, S. M. Brombosz, Z. Xiao, S. Jia, X. C. Xie, and J. Wang, Phys. Rev. X **5**, 031037 (2015).
[43] A. Popescu and L. M. Woods, Adv. Funct. Mater. **22**, 3945 (2012).
[44] K. Behnia, Nat. Nanotechnol. **7**, 488 (2012).
[45] H. Zeng, J. Dai, W. Yao, D. Xiao, and X. Cui, Nat. Nanotechnol. **7**, 490 (2012).
[46] K. F. Mak, K. He, J. Shan, and T. F. Heinz, Nat. Nanotechnol. **7**, 494 (2012).
[47] T. Cao, G. Wang, W. Han, H. Ye, C. Zhu, J. Shi, Q. Niu, P. Tan, E. Wang, B. Liu, and J. Feng, Nat. Commun. **3**, 887 (2012).
[48] M. Ezawa, Phys. Rev. B **89**, 195413 (2014).